

Unraveling electronic structure of GeS through ARPES and its correlation with anisotropic optical and transport behavior

Rahul Paramanik,¹ Tanim Kundu,¹ Soumik Das,¹ Alexey Barinov,² Bikash Das,¹ Sujan Maity,¹ Mainak Palit,¹ Sanjoy Kr Mahatha,^{3,*} and Subhadeep Datta¹

¹*School of Physical Sciences, Indian Association for the Cultivation of Science, 2A & B Raja S. C. Mullick Road, Jadavpur, Kolkata- 700032, India*

²*Sincrotrone Trieste s.c.p.a., 34149 Basovizza, Trieste, Italy*

³*UGC-DAE Consortium for Scientific Research, Khandwa Road, Indore 452001, Madhya Pradesh, India*

Two-dimensional (2D) van der Waals (vdW) materials with lower symmetry (triclinic, monoclinic or orthorhombic) exhibit intrinsic anisotropic in-plane structure desirable for future optoelectronic surface operating devices. Herein, we report one such material, 2D *p*-type semiconductor germanium sulfide (GeS), a group IV monochalcogenide with puckered orthorhombic morphology, in which in-plane optical and transport properties can be correlated with its electronic structure. We systematically investigate the electronic band structure of the bulk GeS with micro-focused angle-resolved photoemission spectroscopy (μ -ARPES) and correspond the charge transport properties using the field-effect transistor (FET) device architecture, and optical anisotropy *via* angle-resolved polarization dependent Raman spectroscopy (ARPRS) on a micron-sized rectangle-shaped exfoliated bulk flake. The experimental valence band dispersion along the two high symmetry directions indicate highly anisotropic in-plane behavior of the charge carrier that agrees well with the density functional theory (DFT) calculations. In addition, we demonstrate the variation of the in-plane hole mobility (ratio ~ 3.4) from the electrical conductivity with gate-sweep in a GeS-on-SiO₂ FET. Moreover, we use the angle-resolved fluctuation of the Raman intensity of the characteristic phonon modes to precisely determine the armchair and zigzag edges of the particular flake. The unique structural motif of GeS with correlated electronic and optical properties are of great interest both for the physical understanding of the all-optical switch and their applications in memory devices.

PACS numbers:

I. INTRODUCTION

Low-symmetry layered materials with their intrinsic in-plane anisotropy have attracted significant attention because of their excellent multifunctional capabilities in next-generation electronics and optoelectronics device physics¹⁻³. The family of in-plane anisotropic 2D materials constitutes black phosphorous⁴, distorted phase of transition metal dichalcogenides like 1T' WTe₂^{5,6}, ReS₂^{7,8}, ReSe₂^{8,9}, transition metal trichalcogenides e.g. TiS₃^{10,11}, puckered structure of PdSe₂^{12,13}, group IV-V compounds such as GeP¹⁴, GeAs¹⁵, newly discovered penta-PdPSe¹⁶ etc. Compared to other materials, this family especially presents unique optical, electrical and thermal properties such as, tunable band gap, anisotropic in-plane optical conductivity, anisotropic light absorption and high mobility, which open up comprehensive performances as polarization sensitive photodetectors^{17,18}, linearly polarized pulse generators¹⁹, polarization sensors²⁰, digital inverters²¹, artificial synaptic devices²², and so on. In spite of so many excellent features, most of them suffer from air-instability and low ON/OFF ratio restricting their applications in future electronics²³. Combining a group IV element (Ge or Si) with group V-VI elements (P, As, S and Se) have been revived with recent advancement incorporating high air-stability, strong in-plane anisotropy, high mobility and excellent device performance^{14,15,24,25}. In particular, these materials are easy to synthesize and highly desirable in the field of solar

cell and photodetector because of their novel functionalities.

Germanium sulfide (GeS) was explored as a 2D monochalcogenide in the family of low-symmetry anisotropic materials²⁴. It belongs to an orthorhombic crystal system and possesses intrinsic anisotropic structural arrangements in armchair and zigzag directions. Angle-dependent photoluminescence spectra and absorption spectroscopy reveal the anisotropic layered structure of GeS²⁴. In recent years, GeS is recognized as a promising candidate in designing high-efficiency solar cells and photodetectors²⁶. However, existing experimental reports mainly focus on the optical anisotropy of GeS^{24,27}, but a comparative study involving detail understanding of both anisotropic optical characterization and electronic structure is still not well-explored.

Herein, we report a detail study of angle-resolved photoemission spectroscopy (ARPES) as well as electronic and optical properties in GeS to investigate the role of in-plane anisotropy in its electronic structure and device performance. Single crystals of GeS were grown via chemical vapor transport (CVT) method. Bulk GeS exhibits *p*-type semiconducting behavior with 1.6 eV indirect band gap. The unit cell of GeS covers two adjacent layers with threefold coordination of each germanium. The anisotropic nature is attributed by its puckered orthorhombic structure with armchair and zigzag atomic arrangements of two different in-plane lattice directions. Field-effect transistor (FET) measurements along two in-

plane orthogonal directions reveal the anisotropic electrical conductivity and transfer characteristics in both dark and illuminated conditions. Electric field driven highest drain current was achieved in the armchair direction with a maximum hole mobility $0.047 \text{ cm}^2/\text{V}\cdot\text{s}$ and ON/OFF ratio $\sim 10^3$. Crystal direction (armchair or zigzag) of a multilayered GeS flake was determined by angle-resolved polarized Raman spectroscopy (ARPRS) which is a widely used tool to identify the crystal orientation for such anisotropic 2D materials²⁸⁻³². Micro-ARPES spectra of freshly cleaved GeS single crystal depicted anisotropic band structure along two orthogonal lattice orientations which is in good agreement with the calculated band structure using density functional theory (DFT). Band dispersions are also different in different orientations. Compared to the previous report³³ our measurement unveil rich and explicit band structure with more sophisticated instrumentation and a comprehensive corroboration with FET measurements, Raman spectroscopy and ab initio DFT calculations.

II. EXPERIMENTAL DETAILS

Synthesis and characterization: Germanium Sulfide (GeS) single crystals were synthesized using chemical vapor transport (CVT) method. Ge (99.95% , Alfa Aesar) and S (99.99% , Alfa Aesar) powders were mixed thoroughly in stoichiometric ratio and Iodine (4 mg/cc) was added as transport agent. The mixture was loaded into a quartz tube which was then evacuated and sealed under a vacuum of 10^{-5} Torr. The sealed tube was placed in a horizontal two-zone tube furnace and the temperature was slowly increased to 873 K and 773 K for source and growth zone, respectively. The furnace was kept at this temperature for 100 hours followed by natural cooling to room temperature. The quartz ampoule was then cracked open in ambient condition to collect the as-grown GeS single crystals.

Single crystal X-ray diffraction (SXRD) was carried out using Bruker APEX II (CCD area detector , Mo $K\alpha$, $\lambda = 0.7107 \text{ \AA}$) at room temperature and the structure solution and refinement was done using the corresponding software packages of the diffractometer. The crystalline phase of the synthesized material was confirmed by room temperature powder x-ray diffraction (XRD Bruker) using Cu- $K\alpha$ radiation followed by the refinement using the Fullprof software. Lattice planes were characterized using Transmission electron microscope (TEM) in a JEOL-JEM-F200 electron microscope by giving an accelerating voltage 200 kV. Elemental analysis was investigated in a Scanning electron microscope (SEM: JEOL JSM-6010LA) by Energy-dispersive spectroscopic (EDS) study.

Angle-resolved photoemission spectroscopy: ARPES measurements were carried out on a freshly cleaved GeS crystal in ultrahigh vacuum at the spectromicroscopy beamline of the Elettra Sincrotrone³⁴ in

Trieste, Italy. The linearly polarized incident radiation was focused through a Schwarzschild objective in order to obtain a spot size of approximately $1 \mu\text{m}$. The spectra were acquired at 93 K with two different photon energies of 27 eV and 74 eV. The scanning stage of the sample was employed for positioning and raster imaging the sample with respect to the fixed photon beam. Photoemission intensity maps were taken by rotating the hemispherical analyzer mounted on a two-axis goniometer. The total energy and angular resolutions were better than 50 meV and 0.35° , respectively.

Device fabrication: For device fabrication, GeS flakes were transferred onto a clean SiO_2/Si substrate by mechanical exfoliation technique using a scotch-tape. Standard electron beam lithography was employed to fabricate cross-shaped field-effect transistor devices. Metal contacts with 80 nm Au were made by thermal evaporation. FET measurements were carried out under dark and white light ($\sim 0.3 \text{ W}$) using a probe station along with Keithley 2450 and 2601B source measure units (SMU).

Angle-resolved polarization Raman spectroscopy: Raman measurements were performed in back-scattering geometry using a Y-J Horiba T64000 Raman spectrometer system equipped with two excitation lasers, a DPSS laser and a He-Ne laser of wavelength 532 nm and 633 nm respectively. The laser beam was focused to approximately $1 \mu\text{m}$ spot size on the sample by using a 50X short-distance (NA= 0.75) microscope objective lens. The laser power was kept below 0.2 mW to avoid damaging the sample. For the polarization-dependence Raman measurements, a half-wave plate was inserted in the path of incident light, and an analyzer was placed before the detector (see Fig. S3). To obtain the parallel polarization configuration, the half wave plate was rotated accordingly such that, the polarization direction of incident and detected beam becomes parallel. The sample was mounted on a custom-made rotation stage, and polarized Raman spectra with different angles were obtained by varying the rotation angle of the sample with a step of 15° .

III. COMPUTATIONAL DETAILS

First principle Density functional theory (DFT) calculations were performed using Vienna Ab initio Simulation Package (VASP)^{35,36} to study the structural, electronic and optical properties of bulk GeS. Projector-augmented-wave (PAW) pseudopotential was employed to describe electron-ion interaction. Generalized gradient approximation (GGA) with the Perdew-Burke-Ernzerhof (PBE)³⁷ functional was considered to incorporate the exchange-correlation effects. The plane wave kinetic energy cut-off was set to 400 eV. The lattice parameters and the atomic coordinates were optimized until the Hellmann-Feynman residual forces were less than 0.001 eV/\AA per atom, and total energy difference criterion for

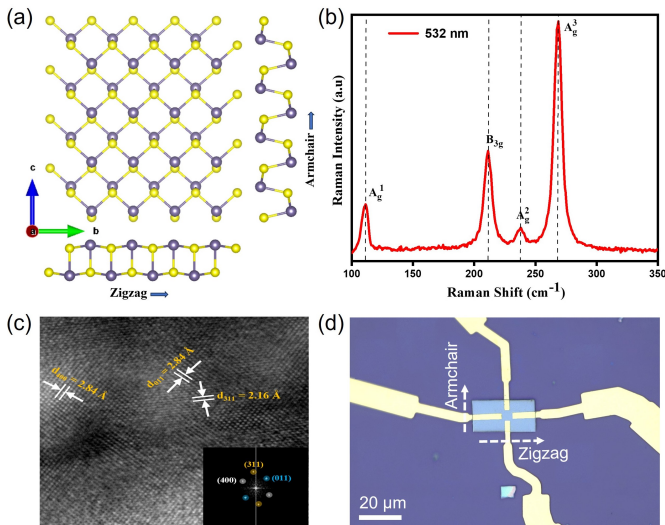


FIG. 1: Germanium sulfide (GeS): (a) Top and side view of the puckered crystal structure showing the armchair and zigzag chain. (b) Ambient Raman spectrum of an exfoliated flake indicating four distinct Raman modes. (c) TEM image of a multilayered flake showing (400), (011), and (311) lattice planes with the interplanar spacings of 2.84, 2.84 and 2.16 Å, respectively. Inset shows the corresponding SAED pattern with the different lattice planes represented by different bright spots. (d) Optical micrograph of a cross-shaped FET device along two orthogonal in-plane orientations.

convergence of electronic self-consistent calculations was set to 10^{-6} eV. For structural relaxations and density of states calculations a $4 \times 6 \times 6$ and $8 \times 12 \times 12$ k-point mesh generated according to the Monkhorst-Pack scheme³⁸, respectively, were employed to sample the irreducible Brillouin zone. To incorporate the optical anisotropy, absorption spectra were simulated in DFT framework implementing VASP³⁹. To visualize the crystal structures VESTA software⁴⁰ was used.

IV. RESULTS AND DISCUSSION

As shown in Fig. 1(a) GeS crystallizes in a 2D-layered structure with orthorhombic space group Pnma (No. 62), with lattice parameters $a = 10.494$ Å, $b = 3.642$ Å, $c = 4.305$ Å and $\alpha = \beta = \gamma = 90^\circ$ as obtained from SXRD refinement. In a single layer of GeS, Ge atoms are covalently bonded with three adjacent sulfur atoms to form a puckered honeycomb structure, and the atomic layers are stacked together by van der Waals interactions. Anisotropy is conceived from this puckered structure of GeS with zigzag and armchair structural arrangements along in-plane lattice directions b and c , respectively. Powder XRD (Fig.S1(a)) and EDS study confirmed the phase and stoichiometry (50.07% of Ge and 49.93% of S) of the as-grown crystals. GeS exhibits four distinct Raman modes ($3A_g$ and B_{1g}) as shown in Fig. 1(b). The lattice planes of GeS crystal were characterized by

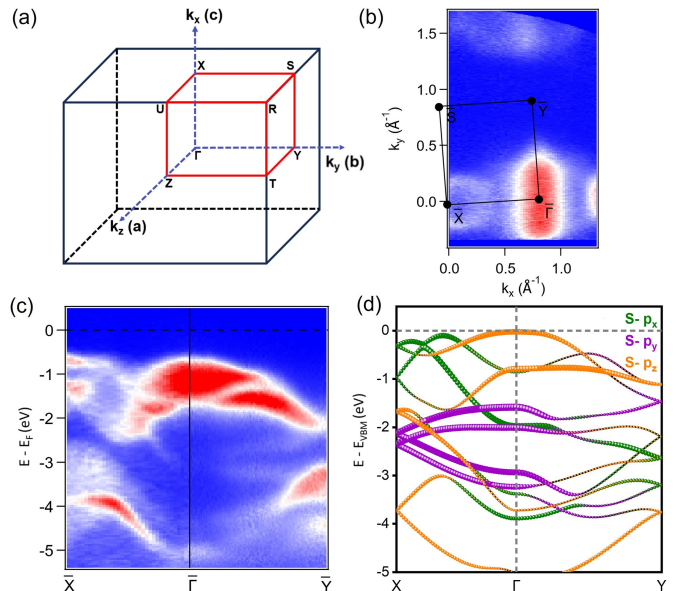


FIG. 2: (a) Schematic of the 3D orthorhombic Brillouin zone of GeS represented with the high symmetry points. (b) Constant energy contour at a binding energy of -1 eV. Rectangular symmetry is consistent with the orthorhombic crystal structure. (c) ARPES spectra of *in situ* cleaved GeS crystal at 93 K using 27 eV photon energy showing anisotropic band dispersion along $\bar{\Gamma} - \bar{X}$ and $\bar{\Gamma} - \bar{Y}$ direction. (d) Orbital projected band structure calculated using DFT framework, well matches with the ARPES spectrum.

Transmission electron microscope (TEM) as shown in Fig. 1(c). The d-spacings were calculated to be 2.84 Å, 2.84 Å and 2.16 Å for planes (400), (011) and (311), respectively which are consistent with that obtained from the crystallographic information file (CIF) extracted from SXRD refinement. Inset of Fig. 1(c) displays the selected area electron diffraction (SAED) pattern where the first order bright spots denote different Bragg planes.

A. Angle-resolved photoemission spectroscopy and density functional theory

To investigate the electronic structure of GeS, angle-resolved photoemission spectroscopy (ARPES) was performed with a μ -focused photon beam using two different photon energies. Fig. 2(a) shows the orthorhombic Brillouin zone (BZ) of GeS, where in-plane lattice axes b and c are considered along k_y and k_x directions, respectively and out-of-plane a -axis is taken along k_z direction. ARPES spectra were taken at two different photon energies to probe the BZ periodicity along k_z direction and locate the desired $k_x - k_y$ surface projection of the 3D BZ in a crude way. Constant energy contour at a binding energy -1 eV (Fig. 2(b)) shows surface-projected rectangular symmetry consistent with an orthorhombic crystal structure. As seen from Fig. 2(b), the intense spot-like feature from the spectral weight of the valence band maxima appears around the Γ point as observed from the

band structure obtained from ARPES using 27 eV photon energy (Fig. 2(c)) as well as DFT (Fig. 2(d)). Additional spot-like feature appears along $\Gamma - X$ direction in the constant energy map which corresponds to another hole valley as observed from band structure also. Parabolic valence band maxima in Fig. 2(c) is situated around a binding energy ~ -0.5 eV. Another two hole valleys towards X direction are energetically very close to VBM. But along $\Gamma - Y$ direction only one valley is observed around ~ 0.5 eV away from VBM. Hole-like valence band is the sharpest using 27 eV photon energy. On the other hand, for 74 eV energy of incident photons the spectra is much weaker and broader (Fig. S2(b)). In contrast to 27 eV energy, some bands at deeper binding energy appear brighter due to the variation of photoemission cross section of the valence bands. Also, the spectra for 74 eV is slightly shifted upwards near the Fermi level due to the out-of-plane dispersion of the bands.

Considering the full energy gap between valence band maxima and conduction band minima is 1.6 eV²⁷, the ARPES result is consistent with the p -type behavior of bulk GeS. The experimental valence bands agree well with the calculated band structure. Fig. 2(d) represents the orbital-projected band structure calculated using DFT (the Fermi level is set to the VBM), where the valence bands near Fermi level are mostly contributed by the $3p$ orbitals of sulfur. The VBM is entirely due to $S-p_z$ orbital and another three hole valleys closed to VBM along two orthogonal directions from Γ point are conceived from $S-p_x$ and p_y orbitals. On the contrary, the conduction bands are generated due to $Ge-4p$ orbitals (Figure S2(c)). An indirect band gap of ~ 1.2 eV is observed with the conduction band minima situated along $\Gamma - Y$ direction, clearly underestimated due to the use of GGA-PBE functional^{41,42}. Another CBM at Γ point is almost degenerate corresponding to a nearly equal direct band gap.

In particular, the most important aspect is that the band structure differ much along two perpendicular in-plane directions from the central Γ point evident from both ARPES and DFT. Henceforth, band dispersion is highly anisotropic which affects their electrical transport as well as optical response. Hole-like valence bands are energetically much closer to the Fermi level along $\Gamma - X$ direction in which there is armchair-like atomic arrangements in real space. This may offer electric field driven hole conduction dominated over the zigzag orientation consistent with our transport measurements. The hole effective masses (m_h^*) were calculated from the experimental band structure by fitting the band dispersions with a parabolic function at the valence band maxima. Fig S2(a) and (b) shows the valence band maxima for armchair (k_x) and zigzag (k_y) directions respectively and the solid green lines indicate the fitted curves. Obtained effective masses along the armchair and zigzag direction are, $0.5 m_e$ and $1.1 m_e$ respectively where m_e is the free electron mass. That is, the effective mass along k_x direction is about 2.1 times lighter than that of the k_y di-

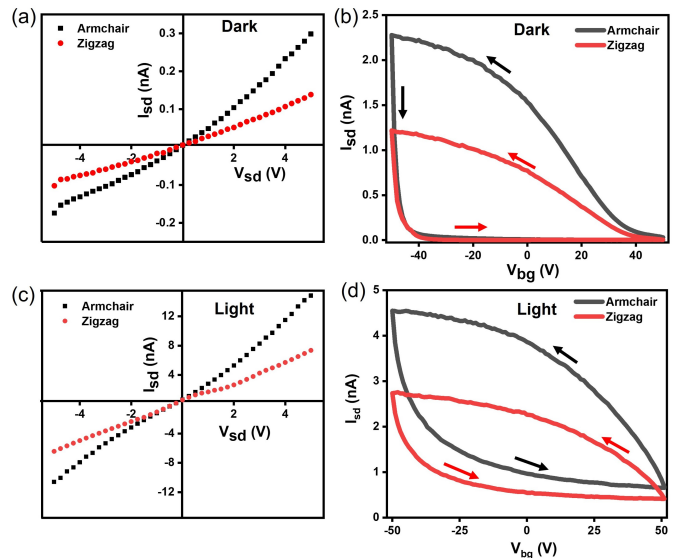


FIG. 3: Two-terminal current-voltage characteristics (I_{sd} vs. V_{sd}) of GeS measured in (a) dark and (c) illuminated condition along armchair (black) and zigzag (red) direction, clearly indicating higher conductance along armchair orientation. Transfer curve (I_{sd} vs. V_{bg}) in back-gated configuration measured in (b) dark and (d) illuminated condition along armchair (black) and zigzag (red) direction. The arrows indicate the direction of hysteresis.

rection. The effective masses (m_h^*) were also calculated from DFT to be $0.42 m_e$ and $0.83 m_e$ along armchair and zigzag directions respectively. The results are consistent with the more dispersive bands along armchair direction resulting in higher curvature, thereby lower effective mass. Lower effective mass corresponds to higher mobility as well, corroborated with the field-effect transport properties. Anisotropic optical absorption spectra were also calculated using the dielectric constants obtained along armchair and zigzag direction (see supplementary section).

B. Field-effect transport measurement

The in-plane anisotropic electrical properties of GeS were investigated through the direction dependent transport measurements. GeS FET devices were fabricated on SiO_2/Si substrate using electron beam lithography followed by Au metal electrode deposition by thermal evaporation. As shown in the optical microscope image Fig. 1(d), four electrodes were fabricated in cross configuration to measure the transport characteristics in two perpendicular directions of multilayered GeS flakes. The armchair and zigzag directions were identified later by angle-resolved Raman scattering experiment described in the next section. The channel size between the electrodes in armchair and zigzag direction were designed to be the same. As shown in Fig. 3(a), I_{sd} (source-drain Current) vs. V_{sd} (source drain voltage) measurement shows clear directional dependence with current along armchair direction being much higher than zigzag direction. Also the

$I_{sd} - V_{sd}$ plots upto $V_{sd} = 5$ V reveals nearly linear behavior indicating good ohmic contact with the electrodes. The variation of the source-drain current (I_{sd}) as a function of back-gate voltage (V_{bg}) with 2 V bias (V_{sd}) was measured along both directions. As shown in Fig. 3(b), I_{sd} decreases with increasing V_{bg} from -50 V to $+50$ V indicating the typical p -type behavior of GeS. This p -type nature is attributed to the presence of Ge vacancies in the crystals or exfoliated flakes resulting in high lying valance band of GeS^{43,44}. The transfer curve also exhibits large anti-clockwise hysteresis which implies the static defect states present in the GeS and SiO₂ interface⁴⁵. The two-probe field-effect mobility (μ_{eff}) was calculated from the linear region of the transfer characteristics using the formula,

$$\mu_{eff,2p} = \frac{L}{WC_{ox}} \frac{dI_{sd}}{dV_{bg}} \frac{1}{V_{sd}} \quad (1)$$

where L and W denote the channel length and channel width of the FET device, C_{ox} is the gate capacitance of the SiO₂ layer which can be estimated as, $C_{ox} = \frac{\epsilon_0 \epsilon_r}{d}$, d being the thickness of the SiO₂ layer and the corresponding dielectric constant $\epsilon_r = 3.9$. The carrier mobilities along armchair and zigzag direction are calculated to be $0.047 \text{ cm}^2 \text{V}^{-1} \text{s}^{-1}$ and $0.014 \text{ cm}^2 \text{V}^{-1} \text{s}^{-1}$, respectively.

Since, GeS also shows excellent photoresponse in visible range, the anisotropic transport properties were also studied after illuminating the device under white light. The $I_{sd} - V_{sd}$ and $I_{sd} - V_{bg}$ curves measured along both directions are shown in Fig. 3(c) and Fig. 3(d), respectively. There is a significant increase in current values compared to dark conditions because of the photocurrent generation in GeS. This effect may be due to the photogating effect which is a special case of photoconductive effect, originating from the high concentration of defect or trap states in semiconductors. Incident photons of sufficient energy generates electron-hole pairs in semiconductor. The trap states inside the defective semiconductor or the surface adsorbates can capture either the photogenerated electrons or holes. In a p -type semiconductor, when the electrons get trapped by defects, only photogenerated holes contribute to the photocurrent and the trapped electrons serve as an additional gating voltage, which effectively modulates the channel conductivity^{24,46,47}. Similar anisotropic transport behavior was observed under white light, and the current ratio between armchair and zigzag direction is nearly equal to that observed in dark condition indicating similar photoresponse along both directions.

C. Angle-resolved polarization Raman spectroscopy

The unit cell of GeS (point group: $D2h$) consists of eight atoms which results in a total 24 vibrational branches. According to the group theory analysis, the irreducible zone-center phonon modes can be expressed as $\Gamma = 4A_g + 2A_u + 2B_{1g} + 4B_{1u} + 4B_{2g} + 2B_{2u} + 2B_{3g} + 4B_{3u}$.

It exhibits 21 optical modes, out of them 2 are inactive, 12 are Raman active ($4A_g$, $2B_{1g}$, $4B_{2g}$, and $2B_{3g}$), and 7 are infrared active ($3B_{1u}$, B_{2u} , and $3B_{3u}$) modes. In the back-scattering Raman geometry, six modes ($4A_g$ mode and $2B_{3g}$ mode) can be detected when crystallographic a axis is parallel to the propagating vector of the laser^{48,49}.

We obtained four characteristic Raman modes at 113 cm^{-1} , 214 cm^{-1} , 239 cm^{-1} , and 270 cm^{-1} excluding the two below 100 cm^{-1} (Fig. 1(b)). The experimental setup for the polarization dependent Raman measurements in back-scattered geometry is schematically shown in Fig. S3(a) and S3(b). In this configuration, the polarization direction of the incident light is described by $\hat{e}_i = (0 \cos\theta \sin\theta)$ with respect to the crystallographic axes as shown in Fig. 1(a), while for scattered light it is written as, $\hat{e}_s = (0 \cos\theta \sin\theta)$ and $\hat{e}_s = (0 \sin\theta \cos\theta)$ for the parallel and cross-polarization configurations, respectively^{28,30}. But, cross polarization doesn't give any extra information, so we have considered only parallel configuration^{50,51}.

Now, the Raman scattering intensities can be expressed in terms of Raman tensor \overleftrightarrow{R}_k as,

$$I_k = |\hat{e}_i \cdot \overleftrightarrow{R}_k \cdot \hat{e}_s|^2 \quad (2)$$

The Raman tensor elements of \overleftrightarrow{R}_k are dependent on the dielectric susceptibility of the material, which has both real and imaginary parts in case of absorptive materials. Hence, the Raman tensor elements should also have complex values as well^{50,52,53}. So, the Raman tensors for A_g and B_{3g} modes can be written in complex form as,

$$\overleftrightarrow{R}_{A_g} = \begin{pmatrix} |a|e^{i\phi_a} & 0 & 0 \\ 0 & |b|e^{i\phi_b} & 0 \\ 0 & 0 & |c|e^{i\phi_c} \end{pmatrix} \quad (3)$$

and

$$\overleftrightarrow{R}_{B_{3g}} = \begin{pmatrix} 0 & 0 & 0 \\ 0 & 0 & |g|e^{i\phi_g} \\ 0 & |g|e^{i\phi_g} & 0 \end{pmatrix} \quad (4)$$

where ϕ is the phase factor.

The corresponding Raman intensities under the parallel polarization configuration are therefore,

$$I_{A_g}^{\parallel} \propto |c|^2 [(\sin^2\theta + \frac{b}{c} |\cos\phi_{bc} \cos^2\theta|)^2 + \frac{b}{c} |\sin^2\phi_{bc} \cos^4\theta|] \quad (5)$$

$$I_{B_{3g}}^{\parallel} \propto |g|^2 \sin^2 2\theta \quad (6)$$

where ϕ_{bc} is the phase difference ($\phi_b - \phi_c$).

We performed the ARPRS measurements on bulk GeS flake using two excitation wavelengths of 532 nm and 633 nm. The intensity of four detected Raman modes were plotted against the angle of rotation (θ) as illustrated in Fig. 4. This angle was primarily set as 0° along the x direction of the flake in lab frame, schematically shown

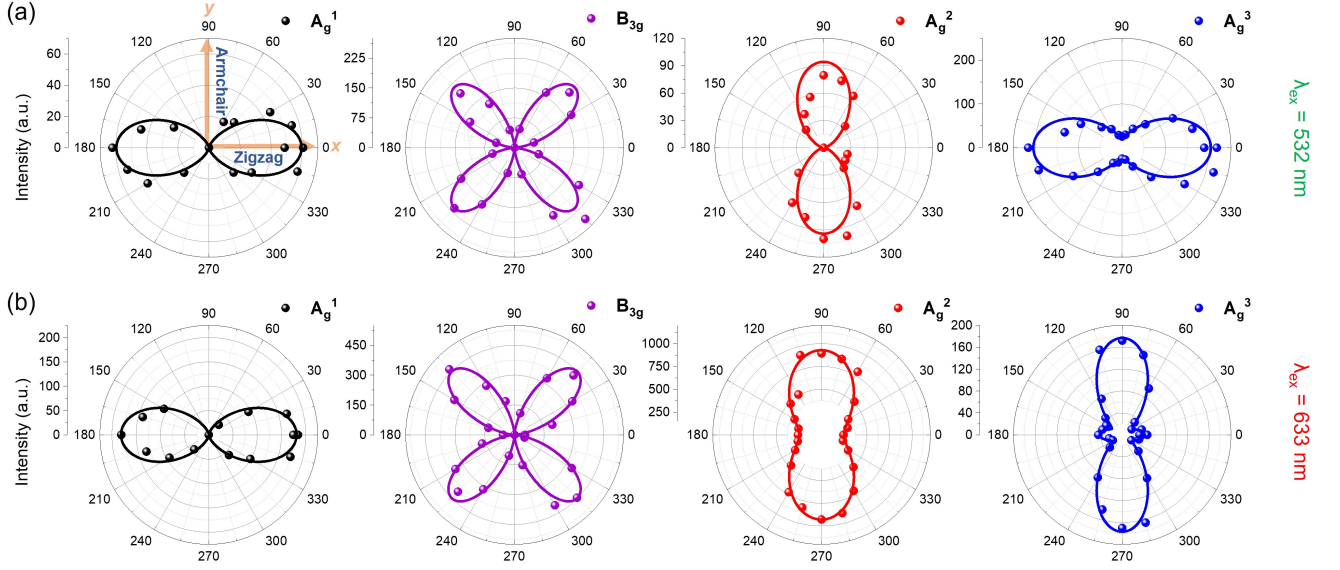


FIG. 4: (a) Polar plots of the Raman peak intensities of four GeS phonon modes A_g^1 , B_{3g} , A_g^2 , and A_g^3 measured in parallel polarization configuration under (a) 532 nm and (b) 633 nm excitation. The experimental results are shown in dots, and the solid lines represent fitting curves obtained from the respective intensity equations given in eq. (5) and (6). Orange arrows in the first figure of (a) denote the crystalline orientation (armchair-zigzag) in lab frame (x-y).

in Fig. S3(b). Different Raman modes reveal different angular dependence which is a direct evidence of the in-plane anisotropy of GeS. The Raman intensity of B_{3g} mode exhibits a periodicity of 90° with the maximum intensity along both $\theta = 0^\circ$ and 90° . Also, the behavior of this mode remains same for both the excitation lasers, because B_{3g} mode does not depend on the phase factor ϕ (see eq. 6). On the other hand, all of the three A_g modes show angular periodicity of 180° . Intensity of A_g^1 mode reaches the maximum value for $\theta = 0^\circ$ and is completely undetectable at $\theta = 90^\circ$. A_g^2 mode possesses two fold symmetry as well, however, in contrast to the A_g^1 mode, the direction of maximum intensity is rotated by 90° . This is because, in \vec{R}_{A_g} , b is greater (smaller) than c for A_g^1 (A_g^2) mode as obtained from the fitting results shown in Table.S1. The behavior of A_g^2 mode gets slightly changed for excitation wavelength 633 nm, where a non zero intensity is observed at the minima Fig. 4(b). A small change in the b/c ratio and the contribution of a minimal phase factor ϕ were noted for the 633 nm excitation by fitting the data with the intensity equations (see Table.S1). On the other hand, the dependence of the A_g^3 mode on the excitation wavelength is substantially larger. There is a 90° shift in the direction of maximum intensity for this mode between the two excitations. Two tiny local maxima also pop up along $\theta = 0^\circ$ for 633 nm. The observed anomalous behavior can be attributed to a significant influence from ϕ . Since, the behavior of A_g^3 mode is completely different under different laser excitation, whereas A_g^1 and A_g^2 have no such change, the determination of armchair or zigzag direction can be possibly

done by comparing the intensities of A_g^1 and A_g^2 modes only.

H. B. Ribeiro *et al.*⁵⁴ observed in their polarization-dependent Raman experiments that the A_g^1 mode has maximum (minimum) intensity along the zigzag (armchair) direction. In a similar manner, our 0° orientation resembles the crystallographic zigzag direction as shown by the orange arrow in the first figure of Fig. 4(a). Our results are also consistent with similar kind of ARPES studies on GeS conducted by D.Tan *et al.*⁵⁵, H. Ouyang *et al.*⁵⁶ and Z. Li *et al.*⁵⁷ as well as for other anisotropic 2D materials with orthorhombic crystal structure^{29,30,50,58}. Related polarization-dependent Raman spectra on exfoliated GeS at the sample's edge showed that either the A_g^1 or A_g^2 mode is strong along the zigzag or armchair direction depending on the respective crystallographic edge and the polarization configuration⁵⁴.

V. CONCLUSIONS

In summary, GeS crystals were successfully synthesized and characterized using basic characterization techniques to confirm the high-quality single crystalline nature. Electronic structure of GeS revealed from ARPES measurement is in well agreement with the band structure calculated from DFT. ARPES study also confirms the p -type semiconducting nature of GeS and the valance band maxima is observed at the Brillouin zone center. Band structure plotted along $X - \Gamma - Y$ direction resembles highly anisotropic band dispersion along

two in-plane crystallographic orientations where the hole-like valance bands along armchair direction being more dispersive and closer to the Fermi level lead to higher hole conductivity. This anisotropic electrical conductivity was confirmed by direction dependent transport measurements on bulk GeS FET devices under both dark and white light condition. The hole mobilities along armchair and zigzag directions were calculated to be $0.047 \text{ cm}^2\text{V}^{-1}\text{s}^{-1}$ and $0.014 \text{ cm}^2\text{V}^{-1}\text{s}^{-1}$ with a ratio of around 3.4 from the transfer curves measured under dark condition. Polarized Raman spectroscopy was employed as an effective and non-destructive technique to identify the armchair and zigzag directions of the GeS FET device. Two excitation lasers were used for polarized Raman study, and the crystal orientation is precisely determined from the A_g^1 and A_g^2 modes having much less dependence on laser wavelength. Altogether, our research constitutes a better understanding towards the optical, vibrational and electrical transport anisotropy coupled with the strongly anisotropic electronic structure of GeS which can be a promising candidate to ignite the future study of multifaceted optoelectronic and nanoelectronic applications.

Acknowledgments

RP would like to thank Mr. Anupam Pal for his input during the growth of the crystal. RP also acknowledges

the financial support from CSIR. TK and SM acknowledge DST-INSPIRE, SDas is grateful to UGC, and BD and MP appreciate IACS for the fellowship. CSS facilities of IACS are greatly acknowledged. TK is thankful to IACS HPC cluster facility. SD acknowledges the financial support from DST-SERB grant No. SCP/2022/000411. SD also acknowledges support from the Technical Research Centre (TRC), IACS, Kolkata. The research leading to μ -ARPES in Elettra, Italy under Proposal No. 20230351 supported by a grant from the Italian Ministry of Foreign Affairs and International Cooperation and the Indian Department of Science & Technology, is greatly acknowledged.

SD, SKM, and RP conceived the project and designed the experiments accordingly. RP prepared the samples and performed their initial characterization together with BD. Device fabrication and modification were carried out by RP, SM and MP. RP performed the electrical measurements and analyzed the data. Polarized Raman spectroscopy and its analysis were performed by RP and SDas. SKM, TK, and SD conceived the ARPES measurements. AB provided the technical support during the beamtime. All DFT calculations were performed by TK discussing with SD. All authors discussed about the results and actively commented on the manuscript written by RP, SKM, and SD.

* Electronic address: sanjoymahatha@gmail.com

- ¹ S. Barraza-Lopez, F. Xia, W. Zhu, H. Wang, Beyond Graphene: Low-Symmetry and Anisotropic 2D Materials. *J. Appl. Phys.*, **128** (14), 140401 (2020).
- ² S. Zhao, B. Dong, H. Wang, H. Wang, Y. Zhang, Z. V. Han and H. Zhang, In-plane anisotropic electronics based on low-symmetry 2D materials: progress and prospects, *Nanoscale Adv.*, **2**, 109-139 (2020).
- ³ J. Zhao, D. Ma, C. Wang, Z. Guo, B. Zhang, J. Li, G. Nie, N. Xie and H. Zhang, Recent advances in anisotropic two-dimensional materials and device applications, *Nano Res.*, **14**, 897-919 (2021).
- ⁴ L. Li, Y. Yu, G. J. Ye, Q. Ge, X. Ou, H. Wu, D. Feng, X. H. Chen, and Y. Zhang, Black phosphorus field-effect transistors, *Nat. Nanotechnol.*, **9**, 372 (2014).
- ⁵ J. Ma, Y. Chen, Z. Han, and W. Li, Strong anisotropic thermal conductivity of monolayer WTe₂, *2D Mater.*, **3**, 045010 (2016).
- ⁶ E. Torun, H. Sahin, S. Cahangirov, A. Rubio, and F. M. Peeters, Anisotropic electronic, mechanical, and optical properties of monolayer WTe₂, *J. Appl. Phys.*, **119**, 074307 (2016).
- ⁷ E. Liu, Y. Fu, Y. Wang, Y. Feng, H. Liu, X. Wan, W. Zhou, B. Wang, L. Shao, C.-H. Ho, Y.-S. Huang, Z. Cao, L. Wang, A. Li, J. Zeng, F. Song, X. Wang, Y. Shi, H. Yuan, H. Y. Hwang, Y. Cui, F. Miao, and D. Xing, Integrated digital inverters based on two-dimensional anisotropic ReS₂ field-effect transistors, *Nat. Commun.*, **6**, 6991 (2015).

- ⁸ J. P. Echeverry and I. C. Gerber, Theoretical investigations of the anisotropic optical properties of distorted 1T ReS₂ and ReSe₂ monolayers, bilayers, and in the bulk limit, *Phys. Rev. B*, **97**, 075123 (2018).
- ⁹ E. Zhang, P. Wang, Z. Li, H. Wang, C. Song, C. Huang, Z.-G. Chen, L. Yang, K. Zhang, S. Lu, W. Wang, S. Liu, H. Fang, X. Zhou, H. Yan, J. Zou, X. Wan, P. Zhou, W. Hu, and F. Xiu, Tunable ambipolar polarization-sensitive photodetectors based on high-anisotropy ReSe₂ nanosheets, *ACS Nano*, **10**, 8067-8077 (2016).
- ¹⁰ A. Khatibi, R. H. Godiksen, S. B. Basuvalingam, D. Pellegrino, A. A. Bol, B. Shokri, and A. G. Curto, Anisotropic infrared light emission from quasi-1D layered TiS₃, *2D Mater.*, **7**, 015022 (2019).
- ¹¹ J. A. Silva-Guillén, E. Canadell, P. Ordejón, F. Guinea, and R. Roldán, Anisotropic features in the electronic structure of the two-dimensional transition metal trichalcogenide TiS₃: Electron doping and plasmons, *2D Mater.*, **4**, 025085 (2017).
- ¹² A. D. Oyedele, S. Yang, L. Liang, A. A. Puzetzy, K. Wang, J. Zhang, P. Yu, P. R. Pudasaini, A. W. Ghosh, Z. Liu, C. M. Rouleau, B. G. Sumpter, M. F. Chisholm, W. Zhou, P. D. Rack, D. B. Geohegan, and K. Xiao, PdSe₂: Pentagonal two-dimensional layers with high air stability for electronics, *J. Am. Chem. Soc.*, **139**, 14090-14097 (2017).
- ¹³ L.-S. Lu, G.-H. Chen, H.-Y. Cheng, C.-P. Chuu, K.-C. Lu, C.-H. Chen, M.-Y. Lu, T.-H. Chuang, D.-H. Wei, W.-C.

- Chueh, W.-B. Jian, M.-Y. Li, Y.-M. Chang, L.-J. Li, and W.-H. Chang, Layer-dependent and in-plane anisotropic properties of low-temperature synthesized few-layer PdSe₂ single crystals, *ACS Nano*, **14**, 4963–4972 (2020).
- ¹⁴ L. Li, W. K. Wang, P. L. Gong, X. D. Zhu, B. Deng, X. Q. Shi, G. Y. Gao, H. Q. Li, T. Y. Zhai, 2D GeP: An Unexploited Low-Symmetry Semiconductor with Strong In-Plane Anisotropy, *Adv. Mater.*, **30**, 1706771 (2018).
- ¹⁵ K. Lee, S. Kamali, T. Ericsson, M. Bellard, and K. Kovnir, GeAs: Highly Anisotropic van der Waals Thermoelectric Material, *Chem. Mater.*, **28**, 8, 2776–2785 (2016).
- ¹⁶ P. Li, J. Zhang, C. Zhu, W. Shen, C. Hu, W. Fu, L. Yan, L. Zhou, L. Zheng, H. Lei, Z. Liu, W. Zhao, P. Gao, P. Yu, G. Yang, Penta-PdPSe: A New 2D Pentagonal Material with Highly In-Plane Optical, Electronic, and Optoelectronic Anisotropy, *Adv. Mater.*, **33**, 2102541 (2021).
- ¹⁷ H. Yuan, X. Liu, F. Afshinmanesh, W. Li, G. Xu, J. Sun, B. Lian, A. G. Curto, G. Ye, Y. Hikita, Z. Shen, S. C. Zhang, X. Chen, M. Brongersma, H. Y. Hwang and Y. Cui, Polarization-sensitive broadband photodetector using a black phosphorus vertical p–n junction, *Nat. Nanotechnol.*, **10**, 707–713 (2015).
- ¹⁸ F. Liu, S. Zheng, X. He, A. Chaturvedi, J. He, W. L. Chow, T. R. Mion, X. Wang, J. Zhou, Q. Fu, H. J. Fan, B. K. Tay, L. Song, R.-H. He, C. Kloc, P. M. Ajayan and Z. Liu, Highly Sensitive Detection of Polarized Light Using Anisotropic 2D ReS₂. *Adv. Funct. Mater.*, **26**, 1169–1177 (2016).
- ¹⁹ D. Li, H. Jussila, L. Karvonen, *et al.*, Polarization and Thickness Dependent Absorption Properties of Black Phosphorus: New Saturable Absorber for Ultrafast Pulse Generation, *Sci Rep*, **5**, 15899 (2015).
- ²⁰ C. Tan, P. Yu, Y. Hu, J. Chen, Y. Huang, Y. Cai, Z. Luo, B. Li, Q. Lu, L. Wang, Z. Liu and H. Zhang, High-Yield Exfoliation of Ultrathin Two-Dimensional Ternary Chalcogenide Nanosheets for Highly Sensitive and Selective Fluorescence DNA Sensors, *J. Am. Chem. Soc.*, **137**, 10430–10436 (2015).
- ²¹ E. Liu, Y. Fu, Y. Wang, Y. Feng, H. Liu, X. Wan, W. Zhou, B. Wang, L. Shao, C. H. Ho, Y. S. Huang, Z. Cao, L. Wang, A. Li, J. Zeng, F. Song, X. Wang, Y. Shi, H. Yuan, H. Y. Hwang, Y. Cui, F. Miao and D. Xing, Integrated digital inverters based on two-dimensional anisotropic ReS₂ field-effect transistors, *Nat. Commun.*, **6**, 6991 (2015).
- ²² H. Tian, Q. Guo, Y. Xie, H. Zhao, C. Li, J. J. Cha, F. Xia and H. Wang, Anisotropic Black Phosphorus Synaptic Device for Neuromorphic Applications, *Adv. Mater.*, **28**, 4991–4997 (2016).
- ²³ O. I. Joshua, A. S. Gary, H. S. J. van der Zant, C.-G. Andres, Environmental instability of few-layer black phosphorus, *2D Mater.*, **2**, 011002 (2015).
- ²⁴ Chen, Z., Hwang, W., Cho, M. *et al.*, In-plane optical and electrical anisotropy in low-symmetry layered GeS microribbons, *NPG Asia Mater.*, **14**, 41 (2022).
- ²⁵ Y. Yang, S.-C. Liu, Y. Wang, M. Long, C.-M. Dai, S. Chen, B. Zhang, Z. Sun, Z. Sun, C. Hu, S. Zhang, L. Tong, G. Zhang, D.-J. Xue, J.-S. Hu, In-Plane Optical Anisotropy of Low-Symmetry 2D GeSe, *Advanced Optical Materials*, **7**, 1801311 (2019).
- ²⁶ H.-C. Hsueh, J.-X. Li, C.-H. Ho, Polarization Photoelectric Conversion in Layered GeS, *Advanced Optical Materials*, **6**, 1701194 (2018).
- ²⁷ A. Tołhoczko, R. Oliva, T. Woźniak, J. Kopaczek, P. Scharocha and R. Kudrawiec, Anisotropic optical properties of GeS investigated by optical absorption and photoreflectance, *Mater. Adv.*, **1**, 1886–1894 (2020).
- ²⁸ B. Xu, N. Mao, Y. Zhao, L. Tong, and J. Zhang, Polarized Raman Spectroscopy for Determining Crystallographic Orientation of Low-Dimensional Materials, *J. Phys. Chem. Lett.*, **12**, 7442–7452 (2021).
- ²⁹ J. Wu, N. Mao, L. Xie, H. Xu, and J. Zhang, Identifying the Crystalline Orientation of Black Phosphorus Using Angle-Resolved Polarized Raman Spectroscopy, *Angew. Chem. Int. Ed.*, **54**, 2366–2369 (2015).
- ³⁰ J. Kim, J. Lee, J. Lee, *et al.*, Anomalous polarization dependence of Raman scattering and crystallographic orientation of black phosphorus, *Nanoscale*, **7**, 18708–18715 (2015).
- ³¹ Y. Choi, K. Kim, S. Y. Lim *et al.*, Complete determination of the crystallographic orientation of ReX₂ (X = S, Se) by polarized Raman spectroscopy, *Nanoscale Horiz.*, **5**, 308–315 (2020).
- ³² M. Zhong, H. Meng, S. Liu, *et al*, In-Plane Optical and Electrical Anisotropy of 2D Black Arsenic, *ACS Nano*, **15**, 1, 1701–1709 (2021).
- ³³ T. Grandke and L. Ley, Angular-resolved uv photoemission and the band structure of GeS, *Phys. Rev. B*, **16**, 832 (1977).
- ³⁴ P. Dudin, P. Lacovig, C. Fava, E. Nicolini, A. Bianco, G. Cauero and A. Barinov, J. Synchrotron Radiat, Angle-resolved photoemission spectroscopy and imaging with a submicrometre probe at the SPECTROMICROSCOPY-3.2L beamline of Elettra, *J. Synchrotron Rad.*, **17**, 445–50 (2010).
- ³⁵ G. Kresse, J. Furthmüller. Efficiency of ab-initio total energy calculations for metals and semiconductors using a plane-wave basis set. *Comp. Mater. Sci.*, **6**, pp. 15–50 (1996).
- ³⁶ G. Kresse, J. Furthmüller. Efficient iterative schemes for ab initio total-energy calculations using a plane-wave basis set. *Phys. Rev. B*, **54**, pp. 11169–11186 (1996).
- ³⁷ Perdew, J. P.; Burke, K.; Ernzerhof, M. Generalized Gradient Approximation Made Simple. *Phys. Rev. Lett.*, **77** (18), 3865 (1996).
- ³⁸ H.J. Monkhorst, J.D. Pack. Special points for Brillouin-zone integrations. *Phys. Rev. B*, **13**, 5188–5192 (1976).
- ³⁹ V. Wang, N. Xu, J.C. Liu, G. Tang, W.T. Geng. VASPKIT: A User-Friendly Interface Facilitating High-Throughput Computing and Analysis Using VASP Code. *Computer Physics Communications*, **267**, 108033 (2021).
- ⁴⁰ K. Momma and F. Izumi. VESTA 3 for three-dimensional visualization of crystal, volumetric and morphology data. *J. Appl. Crystallogr.*, **44**, 1272–1276 (2011).
- ⁴¹ J. P. Perdew and M. Levy, Physical Content of the Exact Kohn-Sham Orbital Energies: Band Gaps and Derivative Discontinuities, *Phys. Rev. Lett.*, **51**, 1884 (1983).
- ⁴² J. M. Crowley, J. Tahir-Kheli, and W. A. Goddard, Resolution of the Band Gap Prediction Problem for Materials Design, *J. Phys. Chem. Lett.*, **7**, 7, 1198–1203 (2016).
- ⁴³ N. Mishra, and G. Makov, Ab initio study of intrinsic point defects in germanium sulfide, *J. Alloys Compd.*, **914**, 165389 (2022).
- ⁴⁴ D. I. Bletskan, I. I. Madyar, S. V. Mikulaninets, and M. Yu. Sichka, Electrical and photoelectric properties of GeS layered crystals grown by different techniques, *Inorg Mater*, **36**, 544–550 (2000).
- ⁴⁵ N. Kaushik, D. M. A. Mackenzie, K. Thakar, N. Goyal, B. Mukherjee, P. Boggild, D. H. Petersen and S. Lodha, Re-

- versible hysteresis inversion in MoS₂ field effect transistors, *npj 2D Mater Appl*, **1**, 34 (2017).
- ⁴⁶ J. Shin and H. Yoo, Photogating Effect-Driven Photodetectors and Their Emerging Applications, *Nanomaterials*, **13**(5), 882 (2023).
- ⁴⁷ D. Tan, W. Zhang, X. Wang, S. koirala, Y. Miyauchi, and K. Matsuda, Polarization-sensitive and broadband germanium sulfide photodetectors with excellent high temperature performance, *Nanoscale*, **9**, 12425-12431 (2017).
- ⁴⁸ J. Jadcak, J. Andrzejewski, J. Debus, C. Ho, and L. Bryja, Resonant Exciton Scattering Reveals Raman Forbidden Phonon Modes in Layered GeS, *J. Phys. Chem. Lett.*, **14**, 17, 3986–3994 (2023).
- ⁴⁹ N. Zawadzka, L. Kipczak, T. Woźniak, *et al.*, Anisotropic Optical and Vibrational Properties of GeS, *Nanomaterials*, **11**(11), 3109 (2021).
- ⁵⁰ H. B. Ribeiro, M. A. Pimenta, C. J. S. de Matos, *et al.*, Unusual Angular Dependence of the Raman Response in Black Phosphorus, *ACS Nano*, **9**, 4, 4270–4276 (2015).
- ⁵¹ X. Ling, S. Huang, E. H. Hasdeo, *et al.*, Anisotropic Electron-Photon and Electron-Phonon Interactions in Black Phosphorus, *Nano Lett.*, **16**, 4, 2260–2267 (2016).
- ⁵² G. C. Resende1, G. A. S. Ribeiro, O. J. Silveira *et al.*, Origin of the complex Raman tensor elements in single-layer triclinic ReSe₂, *2D Mater.*, **8**, 025002 (2021).
- ⁵³ T. Strach, J. Brunen, B. Lederle, J. Zegenhagen, and M. Cardona, Determination of the phase difference between the Raman tensor elements of the A_{1g}-like phonons in SmBa₂Cu₃O_{7-δ}, *Phys. Rev. B*, **57**, 1292 (1998).
- ⁵⁴ H. B. Ribeiro, S. L. L. M. Ramos, L. Seixas, C. J. S. de Matos, and M. A. Pimenta, Edge phonons in layered orthorhombic GeS and GeSe monochalcogenides, *Phys. Rev. B*, **100**, 094301 (2019).
- ⁵⁵ D. Tan, H. E. Lim, F. Wang, N. B. Mohamed, S. Mouri, W. Zhang, Y. Miyauchi, M. Ohfuchi and K. Matsuda, Anisotropic optical and electronic properties of two-dimensional layered germanium sulfide, *Nano Res.*, **10**, 546–555 (2017).
- ⁵⁶ H. Ouyang, C. Zhang, Q. Liu, *et al.*, Polarization-tunable nonlinear absorption patterns from saturated absorption to reverse saturated absorption in anisotropic GeS flake and an application of all-optical switching, *Sci. China Mater.*, **63**, 1489–1502 (2020).
- ⁵⁷ Z. Li, Y. Yang, X. Wang, W. Shi, D. Xue, and J. Hu, Three-Dimensional Optical Anisotropy of Low-Symmetry Layered GeS, *ACS Appl. Mater. Interfaces*, **11**, 27, 24247–24253 (2019).
- ⁵⁸ J. Xia, X. Li, X. Huang, N. Mao, D. Zhu, L. Wang, H. Xuc and X. Meng, Physical vapor deposition synthesis of two-dimensional orthorhombic SnS flakes with strong angle/temperature-dependent Raman responses, *Nanoscale*, **8**, 2063-2070 (2016).

Supplementary Material for 'Unraveling electronic structure of GeS through ARPES and its correlation with anisotropic optical and transport behavior'

Rahul Paramanik,¹ Tanima Kundu,¹ Soumik Das,¹ Alexey Barinov,² Bikash Das,¹
Sujan Maity,¹ Mainak Palit,¹ Sanjoy Kr Mahatha,^{3,*} and Subhadeep Datta¹

¹*School of Physical Sciences, Indian Association for the Cultivation of Science,
2A & B Raja S. C. Mullick Road, Jadavpur, Kolkata- 700032, India*

²*Sincrotrone Trieste s.c.p.a., 34149 Basovizza, Trieste, Italy*

³*UGC-DAE Consortium for Scientific Research,
Khandwa Road, Indore 452001, Madhya Pradesh, India*

* sanjoymahatha@gmail.com

I. RAMAN TENSOR NOTATIONS

Various coordinate notations have been used in the literature. For example, some use a as armchair, b as zigzag, c as out-of-plane directions [1, 2]; some use a as armchair, c as zigzag, b as out-of-plane direction [3] or b as armchair, c as zigzag, a as out-of-plane [4]. Notably, different notations result in distinct Raman mode representations, especially for B_g mode. For instance, the B_g mode is represented as B_{1g} , B_{2g} , and B_{3g} , respectively, if we choose c , b , and a as the out-of-plane direction [5]. For Orthorhombic GeS crystallizing in $Pnma$ space group, a is the out-of-plane direction, b is zigzag, and c is armchair direction.

$$\overleftrightarrow{R}_{A_g} = \begin{pmatrix} a & 0 & 0 \\ 0 & b & 0 \\ 0 & 0 & c \end{pmatrix}, \overleftrightarrow{R}_{B_{1g}} = \begin{pmatrix} 0 & d & 0 \\ d & 0 & 0 \\ 0 & 0 & 0 \end{pmatrix}, \overleftrightarrow{R}_{B_{2g}} = \begin{pmatrix} 0 & 0 & f \\ 0 & 0 & 0 \\ f & 0 & 0 \end{pmatrix}, \overleftrightarrow{R}_{B_{3g}} = \begin{pmatrix} 0 & 0 & 0 \\ 0 & 0 & g \\ 0 & g & 0 \end{pmatrix} \quad (1)$$

TABLE S1. Fitting parameters for the polar plots of GeS Raman modes

Raman Modes	532 nm				633nm			
	b	c	b/c	ϕ	b	c	b/c	ϕ
A_g^1	7.7 ± 0.2	0.5 ± 0.2	15.1 ± 5.9	0	13.5 ± 0.3	1.6 ± 0.8	8.3 ± 4.3	0
A_g^2	1.4 ± 0.7	9.7 ± 0.3	0.1 ± 0.1	0	15.7 ± 0.6	30.5 ± 0.4	0.5 ± 0.1	34.0 ± 11.8
A_g^3	14.3 ± 0.2	5.2 ± 0.6	2.7 ± 0.3	52.0 ± 8.1	6.4 ± 0.2	13.3 ± 0.1	0.5 ± 0.1	112.0 ± 4.3
	g				g			
B_{3g}	14.7 ± 0.2				21.2 ± 0.3			

II. ABSORPTION SPECTROSCOPY

The optical-absorption spectrum of GeS was calculated using density functional theory to reveal the anisotropy in electronic structure, as shown in Fig. S2(d). The absorption

coefficient α_x begins to increase from ~ 1.6 eV indicating that the optical-absorption edge is around 1.6 eV which corresponds to the transition marked by blue arrow in Fig. S2(c). In contrast, the optical absorption edge along y direction (α_y) is at ~ 1.75 eV corresponding to the transition marked by green arrow in Fig. S2(c). Also, the absorption intensity is weak compared to α_x within the same energy regime. The absorption coefficient reaches a relatively larger value of 3.0×10^5 at around 2.5 eV. This large value of the absorption coefficient comes from the optically allowed transition above 1.6 eV. The calculated value of the optical-absorption edge is consistent with the previously reported experimental absorption spectroscopy measurements of bulk GeS [6, 7].

-
- [1] F. Xia, H. Wang, and Y. Jia, Rediscovering black phosphorus as an anisotropic layered material for optoelectronics and electronics, *Nat Commun*, **5**, 4458 (2014).
 - [2] H. Yuan, X. Liu, F. Afshinmanesh *et al*, Polarization-sensitive broadband photodetector using a black phosphorus vertical p–n junction. *Nature Nanotech*, **10**, 707–713 (2015).
 - [3] H. B. Ribeiro, M. A. Pimenta, C. J. S. de Matos *et al*, Unusual Angular Dependence of the Raman Response in Black Phosphorus, *ACS Nano*, **9**, 4, 4270–4276 (2015).
 - [4] S. Sugai, and I. Shirovani, Raman and infrared reflection spectroscopy in black phosphorus, *Solid State Commun.*, **53** (9), 753–755 (1985).
 - [5] X. Ling, S. Huang, E. H. Hasdeo *et al*, Anisotropic Electron-Photon and Electron-Phonon Interactions in Black Phosphorus, *Nano Lett.*, **16**, 4, 2260–2267 (2016).
 - [6] D. Tan, H. E. Lim, F. Wang, N. B. Mohamed, S. Mouri, W. Zhang, Y. Miyauchi, M. Ohfuchi and K. Matsuda, Anisotropic optical and electronic properties of two-dimensional layered germanium sulfide, *Nano Res.*, **10**, 546–555 (2017)..
 - [7] A. Tołłoczko, R. Oliva, T. Woźniak, J. Kopaczek, P. Scharocha and R. Kudrawiec, Anisotropic optical properties of GeS investigated by optical absorption and photoreflectance, *Mater. Adv.*, **1**, 1886-1894 (2020).

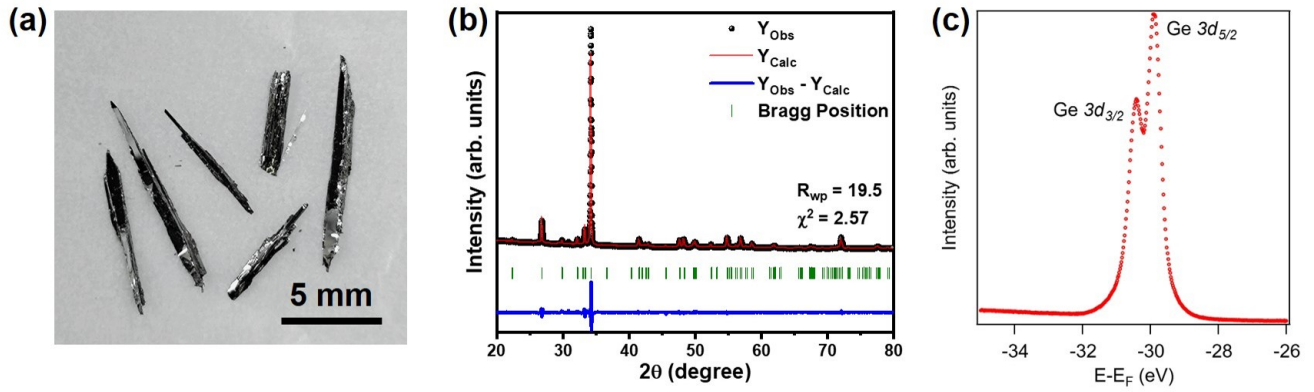


FIG. S1. (a) Optical image of the as-grown GeS single crystals. (b) Rietveld refined powder X-ray diffraction pattern confirming the orthorhombic phase of GeS. (c) Core level photoemission spectrum of Ge measured using synchrotron beamline source.

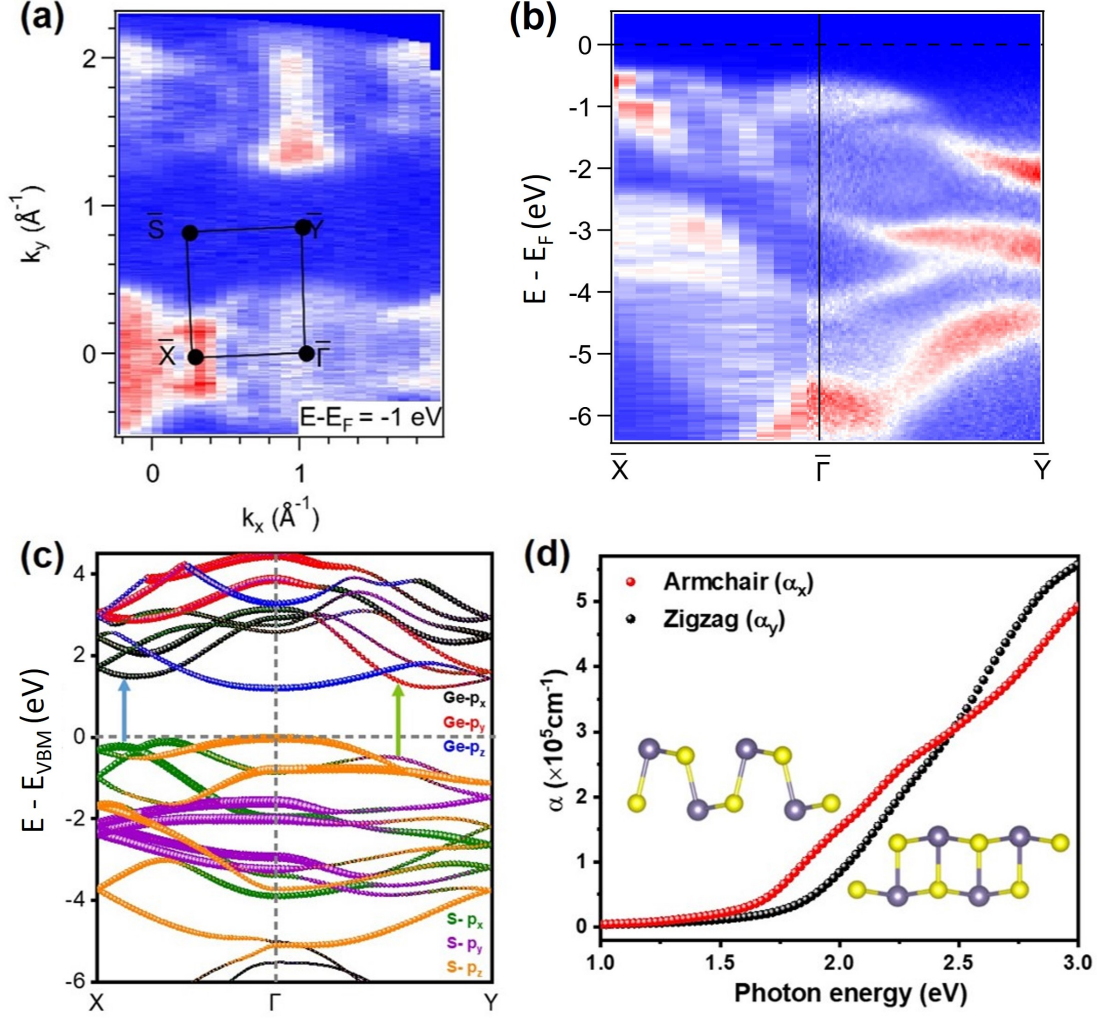


FIG. S2. ARPES (photon energy 74 eV) and DFT: (a) Constant energy contour at a binding energy of -1 eV. Rectangular symmetry is consistent with the orthorhombic crystal structure. (b) ARPES spectra of *in situ* cleaved GeS crystal at 93 K showing anisotropic band dispersion along $\bar{\Gamma} - \bar{X}$ and $\bar{\Gamma} - \bar{Y}$ direction. (c) Orbital projected band structure calculated using DFT framework depicting a band gap of 1.2 eV. (d) Calculated absorption coefficients of GeS as a function of photon energy along armchair and zigzag crystal orientation.

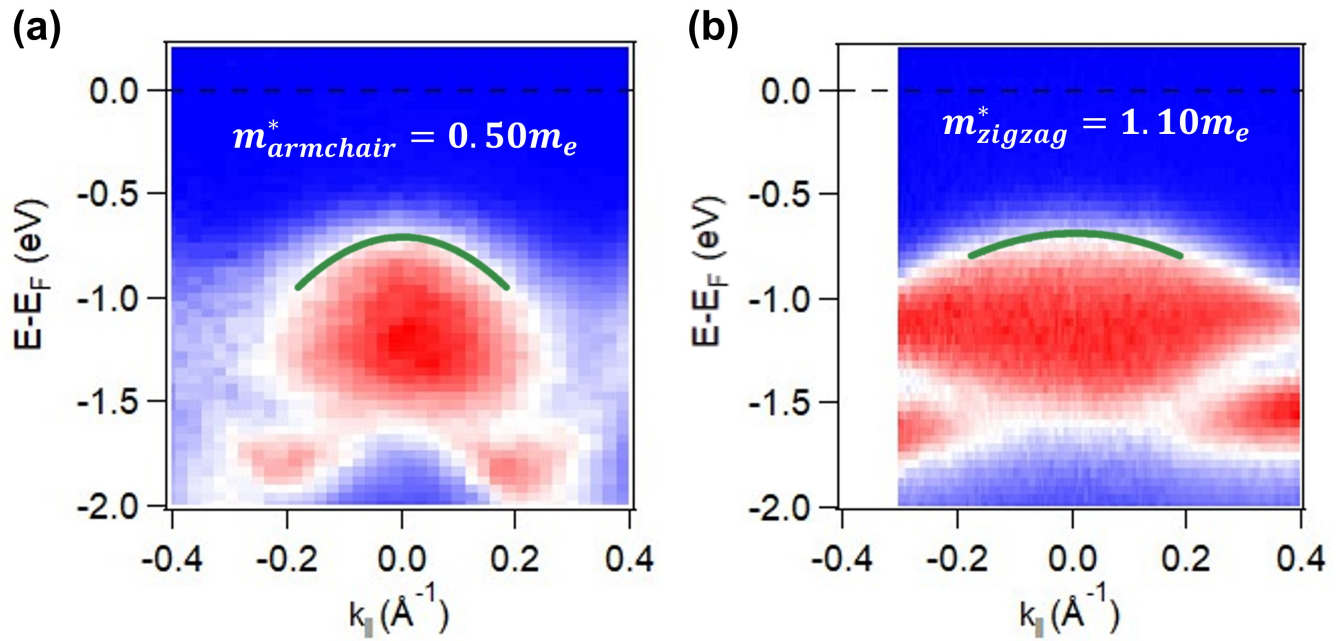


FIG. S3. High symmetric cuts along (a) armchair (k_x) and (b) zigzag (k_y) directions. The dotted lines in (a,b) depict the parabolic fit to the top-most valence bands. The effective masses of hole carriers along different orientations extracted from the fitting equations are shown in the figures.

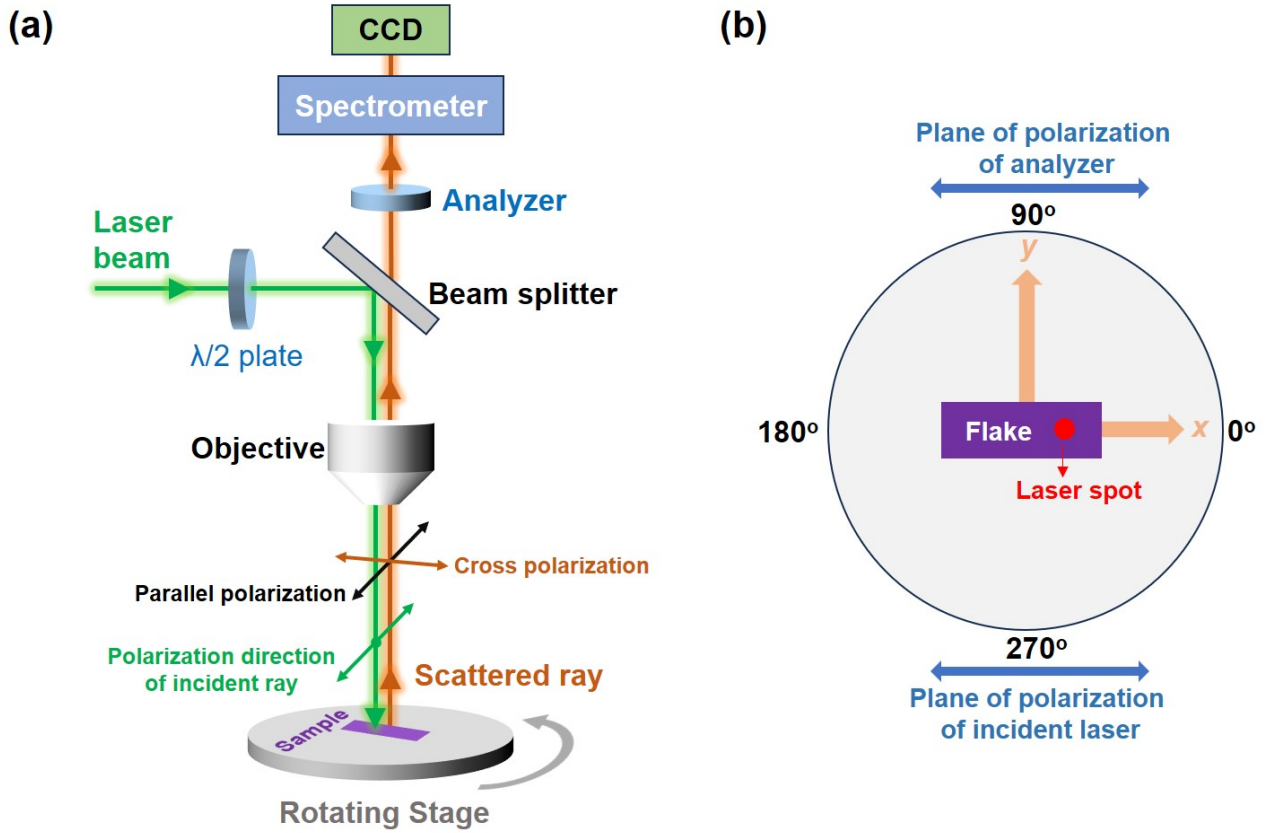


FIG. S4. Schematic of (a) the experimental setup of angle-resolved polarization Raman spectroscopy. (b) Top view of the parallel-polarization Raman setup in lab-frame.

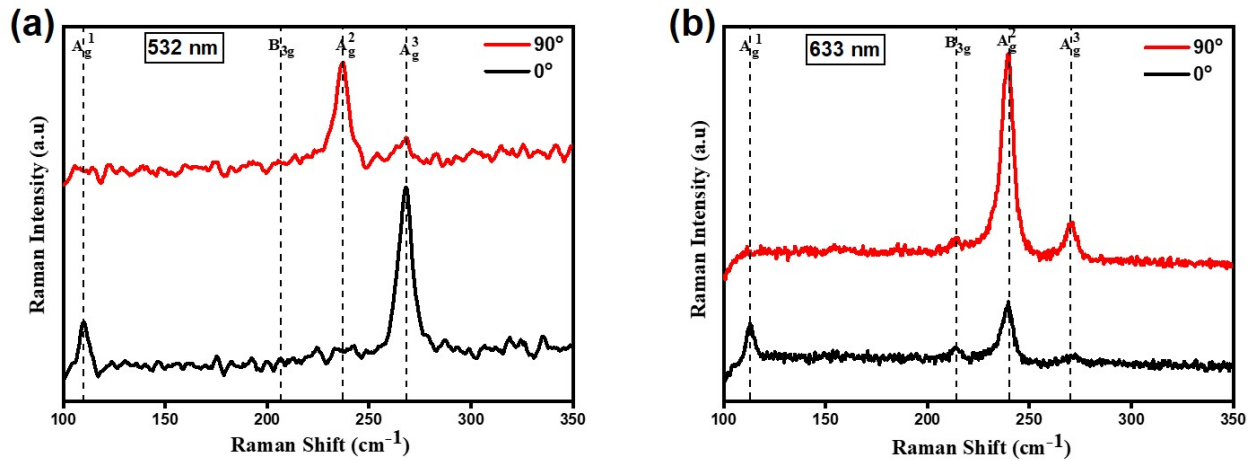


FIG. S5. (a) Polarized Raman spectra of GeS at 0° and 90° angle for (a) 532 nm, (b) 633 nm excitation under parallel polarization configuration.